Clim. Past Discuss., 7, 199–240, 2011
www.clim-past-discuss.net/7/199/2011/
doi:10.5194/cpd-7-199-2011

Climate of the Past Discussions

Implications of the permanent El Niño teleconnection "blueprint" for past global and North American hydroclimatology

A. Goldner[1], M. Huber[1], N. Diffenbaugh[2], and R. Caballero[3]

[1]Earth and Atmospheric Sciences, Purdue University, USA
[2]School Earth of Sciences, Stanford University, USA
[3]Meteorology and Climate Centre, School of Mathematical Sciences, University College Dublin, Dublin, Ireland

Received: 6 December 2010 – Accepted: 20 December 2010 – Published: 17 January 2011

Correspondence to: A. Goldner (agoldner@purdue.edu)

Published by Copernicus Publications on behalf of the European Geosciences Union.

Abstract

Substantial evidence exists for wetter-than-modern continental conditions in past warm climates. This is in apparent conflict with the robust global prediction for future climate change of a northward expansion of the subtropical dry zones that should drive aridification of many semiarid regions. Areas of expected aridification include much of Western North America, where extensive paleoenvironmental records from North America point to wetter conditions before the onset of Quaternary ice ages. It has been proposed that climates previous to the early Pliocene may have been characterized as being in a state with warmer-than-modern eastern equatorial sea surface temperatures (SSTs). Because Equatorial Pacific SSTs exert strong controls on mid-latitude atmospheric circulation and the global hydrologic cycle, the teleconnected response from this permanent El Niño-like mean state has been proposed as a useful analogue model, or "blueprint", for understanding global climatological and hydrological anomalies in the past. The present study quantitatively explores the implications of this blueprint for past climates, using a global climate model (CAM3.0) and a nested high-resolution climate model (RegCM3) to study the hydrologic impacts of a permanent El Niño on global and North American climate. We find that the global circulation response to a permanent El Niño resembles a large, long El Niño event. However, this state also exhibits equatorial super-rotation, which would represent a fundamental change to the tropical circulations. We also find intensification and southward drift in winter storm tracks in the Pacific, which affects precipitation and temperature over the mid-latitudes via large shifts in atmospheric circulation. In addition, summertime precipitation increases over the majority of the continental United States, with these increases likely controlled by shifts in the subtropical jet and secondary atmospheric feedbacks. Based on these results, we conclude that a permanent El Niño is a good explanation of the Pre-Quaternary wetter-than-modern conditions observed in paleo proxy records, particularly over the Western United States.

CPD
7, 199–240, 2011

1 Introduction

The Miocene and Pliocene were 2–3 °C warmer globally than modern, and wetter, with a reduced meridional temperature gradient, despite the fact that continental configurations and atmospheric carbon dioxide levels were similar to modern values (Axelrod, 1997; Wolfe, 1994; Pagani et al., 1999; Pearson and Palmer, 2000; Lyle et al., 2008; Kurschner et al., 2009). These warmer and wetter conditions occurred within the context of a long-term Cenozoic cooling (e.g., Zachos et al., 2001) with climate transitioning toward the relatively arid and cool modern conditions in a stepped fashion from the Miocene into the Pliocene (Cerling et al., 1997; Pagani et al., 1999; Zachos et al., 2001; Fortelius et al., 2002; Huang et al., 2007). It is potentially informative to investigate the changes in climate in these intervals, as they may hold clues to the climate dynamics that will shape the response to elevated greenhouse forcing in the coming decades (Crowley, 1996; Raymo et al., 1996; Ravelo et al., 2004).

Global climate model ensembles of future global warming show a poleward expansion of the margin of the Hadley cell and associated storm track moisture flux divergence, resulting in increased aridity near subtropical margins such as Southwestern North America (Held and Soden, 2006; Seager et al., 2007; Seager and Vecchi, 2010; O'Gorman and Schneider, 2010). This response to elevated greenhouse forcing appears at odds with widespread evidence for wetter-than-modern conditions in the pre-Quaternary warm periods, including many semiarid regions. Here we focus on the hydroclimate of one such region: Western North America.

One potential resolution to this regional aridity paradox is the possibility that these observed wet regions were under the influence of remote impacts from the Equatorial Pacific. Atmospheric teleconnections associated with tropical SST anomalies influence the hydrologic cycle over the Western United States on interannual-to-millennial time scales (Cook et al., 2004; Cole et al., 2002; Held and Soden, 2006; Pierrehumbert, 2002; Fedorov et al., 2000; Chiang, 2009; Seager and Vecchi, 2010). Whereas there is a general scientific consensus that a warmer world is associated with a wider

CPD
7, 199–240, 2011

Hadley cell and displaced jet, data, theory, and models show a variable response of zonal sea level pressure and SST gradients in the Pacific, implying that the future state of the Equatorial Pacific is uncertain (Karnauskas et al., 2009; Sang-Wook et al., 2009). Indeed, while current teleconnection patterns suggest that the response of the tropical Pacific to global warming is likely critical in determining mid-latitude climate change,there is currently no consensus from observations, theory or models about whether a globally warmer world requires –or results in –a tropical Pacific mean state that is closer to a La Niña- or El Niño-like configuration.

Paleoclimate reconstructions for the Pliocene and Miocene indicate that these periods may have exhibited a permanent El Niño state in the tropical Pacific (Ravelo et al., 2004; Brierley et al., 2009; Wara et al., 2005; Fedorov et al., 2006; Dekens et al., 2007, 2008). Molnar and Cane (2002) argued that a permanent El Niño-like SST distribution might have had global, teleconnected effects on temperature and effective moisture that resemble those noted from proxy records in the Pliocene, thus providing a "blueprint" to explain many of the observed features of past climates.

A limited number of permanent El Niño simulations have been conducted in order to better understand ocean-atmosphere interactions, including those operating during past warm periods in Earths history. Barreiro et al. (2006) used observational El Niño composites to better understand the high-and mid-latitude temperature changes resulting from ENSO teleconnections. Vizcaino et al. (2010) increased the ocean heat transport in a slab ocean simulation, producing an El Niño-like state to explore El Niño teleconnections over the Northern Hemisphere. Shukla et al. (2009) imposed the large 1997/98 El Niño with Pliocene boundary conditions to explore global teleconnections within the Pliocene interval. Finally, to further explore the hypothesis suggested by Molnar and Cane (2002), Huybers and Molnar (2007) used modern empirical estimates of high latitude temperature driven by El Niño events to understand the teleconnected response the Equatorial Pacific SSTs may have had on the gradual cooling in the high latitudes over the late Pliocene. We are going to build off previous permanent El Niño simulations by focusing on the hydroclimatological aspects of the permanent El Niño

CPD
7, 199–240, 2011

blueprint and the degree to which past SST changes may have substantially perturbed global and regional effective moisture regimes. This study will explore the hydrologic cycle teleconnections driven by a permanent El Niño using a global and a higher resolution regional climate model. We empasize North America in the analysis because it is both likely to be sensitive to tropical changes and a rich source of paleoclimate proxy data.

Here we focus on the hydroclimatic aspects of the permanent El Niño blueprint, and the degree to which such SST changes may perturb global and regional effective moisture regimes. We emphasize North America in the analysis both because it is a rich source of terrestrial paleoclimate proxy data, and because modern teleconnections suggest that it is likely to be highly sensitive to tropical SST changes. Indeed, many of hydroclimatic features important for cold-season climate in North America can be understood by analyzing large-scale circulation features (Horel and Wallace, 1981; Trenberth et al., 2008). Alternatively, the warm-season atmospheric circulation is sensitive to regional- and local-scale processes that are not well resolved in global climate models (e.g., Castro et al., 2001; Diffenbaugh et al., 2005; Diffenbaugh and Ashfaq, 2010). Consequently, in this study we explore the teleconnections driven by a permanent El Niño using both a global climate model and a nested high-resolution climate model. To our knowledge, no climate modeling study has yet investigated how a permanent El Niño affects the hydroclimate of Western North American using a high-resolution climate modeling system.

This study is broken down into 5 sections. Section 2 describes model and methodology. Section 3 describes the global and regional temperature and precipitation patterns driven by a permanent El Niño and how a permanent El Niño affects seasonal circulation patterns. Section 4 includes the discussion and Sect. 5 describes the conclusions.

CPD
7, 199–240, 2011

2 Methods

We perform a series of prescribed-SST simulations using the National Center for Atmospheric Research (NCAR) Community Atmosphere Model (CAM3.0). CAM3.0 serves as the atmospheric component of the NCAR CCSM3 atmosphere-ocean general circulation model (AOGCM) (Collins et al., 2006). CAM3.0 employs the Hack convection scheme and spectral Eulerian dynamical core (Hack et al., 2006). We run CAM3.0 at T85 spectral truncation, which is approximately 1.2° resolution in the horizontal. CAM3.0 captures the observed atmosphere response to ENSO forcing even when the ENSO signal is incorrect (Joseph and Nigam, 2006), including the far-field mid-latitude atmospheric response. CAM3.0 also represents major features of the global hydrological cycle, even when responding to low frequency ENSO forcing (Hurrell et al., 2006; Hack et al., 2006). When run at T85 resolution, CAM3.0 shows significant improvements over the lower resolution version of CAM3.0, including improved representation of the monsoon circulation associated with improved resolution of topographic features (Meehl et al., 2006).

We create a permanent El Niño-like SST boundary condition by low-pass filtering the historical observed SST field. This filtering retains variability longer than 3 years and SST anomalies that are highly correlated with the Niño3.4 low-pass-filtered index from the ERA40 reanalysis. We then add the low-pass-filtered SST anomalies to the NCAR climatological SST distribution over the entire ocean (Hurrell and Trenberth, 1999). The permanent El Niño SST anomaly can be seen in the surface temperature anomaly in Fig. 1. This is a highly idealized permanent El Niño and the anomalies are constant in all months. Sea ice properties (fraction and thickness) in the specified SST version of CAM3 are normally derived from SST, but are unchanged in our simulations because we are not interested here on high latitude features.

The resulting SST patterns are broadly consistent with proxy based SST reconstructed for the Pliocene but are not meant to faithfully reproduce the details of the time interval (Wara et al., 2005; Dekens et al., 2008). Further, we use modern sea

CPD
7, 199–240, 2011

ice distribution, land-sea orography, continental topography, orbital configuration and land cover boundary conditions. While these non-SST influences were undoubtedly important in shaping features of the climate in past time periods (e.g., Haywood et al., 2004; Herold et al., 2008; You et al., 2009), our goal in the current study is to isolate the dominant patterns that may be forced by permanent El Niño-like conditions in any past or future time period.

The GCM simulations were run for 50 years, with the last 20 used for the climatologies. All differences discussed are significant as the greater than 95% confidence interval based on a students T-test. In our simulations, the El Niño test case will be called NINO and the control case will be referred to as MODERN.

2.1 High-resolution nested climate model simulations

In addition to the GCM experiments, we also nest the ICTP RegCM3 climate model (Pal et al., 2007) within CAM3.0 in order to test the role of fine-scale climate processes in shaping the regional hydroclimatic response to permanent El Niño-like SSTs. RegCM3 is a hydrostatic, sigma coordinate, primitive equation nested climate model. We employ the grid and parameterization options of Diffenbaugh et al. (2006) and Pal et al. (2000). In this configuration, the equal-area (horizontal) grid encompasses the continental United States, with 55 km resolution in the horizontal and 18 levels in the vertical. We generate two RegCM3 simulations, one nested in the CAM3.0 modern control simulation, and one in the CAM3.0 NINO simulation. We integrate the RegCM3 simulations for 40 model years, with the last 20 used for analysis.

RegCM3 is able to capture the seasonal patterns of temperature and precipitation seen in observational data (Diffenbaugh et al., 2006; Walker and Diffenbaugh, 2009; Diffenbaugh and Ashfaq, 2010), as well as the patterns of the hot, cold, and wet tails of the daily temperature and precipitation distributions (Walker and Diffenbaugh, 2009) and the pattern and magnitude of the historical hottest-season (Diffenbaugh and Ashfaq, 2010). RegCM3 also accurately simulates the mean and trends in peak snowmelt-runoff timing in the Western US (Rauscher et al., 2008), as well as the pattern of

CPD
7, 199–240, 2011

Convective Available Potential Energy (CAPE) in the US (Trapp et al., 2007).

Further, because of its higher resolution representation of the atmosphere and land surface, RegCM3 is able to better resolve fine-scale atmospheric features and climate system feedbacks than the lower resolution GCM (Diffenbaugh et al., 2005; Rauscher et al., 2008; Ashfaq et al., 2009). As one illustration, the differences in the simulation of baseline precipitation over the topographically complex Western US can be clearly seen between CAM3.0 and RegCM3 in Fig. 2. These differences are important for the cold season, when storm systems enter the United States through the West Coast, and for the warm season, when precipitation is dominated by convective processes.

3 Permanent El Niño results

3.1 Changes in global and annual means

By design, the permanent El Niño SST pattern is consistent with a canonical El Niño as seen in the model simulated NINO minus MODERN surface temperature anomaly (Fig. 1a). For reference, strong El Niño years usually exhibit an average of 2 to 3 °C deviation from the normal SST pattern in the Eastern Pacific (Trenberth and Hoar, 1997), in close agreement to our El Niño SSTs.

The permanent El Niño conditions increase simulated global mean temperature by 0.272 °C. This global temperature anomaly is similar to the approximately 0.2 °C anomaly seen in the strong El Niño of 1997/1998 (Hansen et al., 2006). As expected, the teleconnected terrestrial temperature response to the imposed El Niño SST anomaly closely resembles the pattern found in reanalysis products such as ERA-40 during large El Niño events (Diaz et al., 2001). In addition, the high-latitude warmth seen over Canada and Alaska agrees spatially with the results presented in the permanent El Niño simulation Barreiro et al. (2006). Further, anomalies between the NINO and MODERN cases result in meridional stationary heat and water transport anomalies over the Pacific Northwest and Canada that transports more heat and water poleward

CPD
7, 199–240, 2011

(Figure not shown). These results agree with the meridional temperature and moisture advection anomalies presented in the permanent El Niño experiment of Vizcaino et al. (2010).

Global mean precipitation for the MODERN case is 103.76 cm year^{-1}, which is in close agreement with the recorded global precipitation mean of 102.2 cm year^{-1} (Huffman et al., 1997; Xie et al., 1997). Globally averaged precipitation increases by 2.7% in the NINO case (relative to the MODERN case), as compared to 0.2% change for typical El Niño events (Dai and Wigley, 2000). When normalized by global mean temperature change, the percentage change in precipitation is 9.9% per ˚C, compared to 3.2% per ˚C for the typical change in temperature due to El Niño events (Trenberth et al., 2002). Given that the value in CAM3 is 3.3% per ˚C (Held and Soden, 2006) in response to increased greenhouse gas concentrations, permanent El Niño forcing is much more effective at increasing precipitation globally than can be expected from simple thermodynamic and radiative arguments.

Annual precipitation increases are seen in Central South America, Eastern Australia, Southern Africa, and over Europe in the NINO case (relative to MODERN) (Fig. 1b). Annual precipitation decreases are seen in Northern South America, the Central East African coast, and Southern India (Fig. 1b). The spatial pattern of the precipitation anomalies (Fig. 1b) agrees with previous research analyzing satellite and rain gauge data (Dai and Wigley, 2000), and is consistent with the blueprint argument (Molnar and Cane, 2002).

3.2 Annual-mean planetary-scale circulation and superrotation

In passing from the MODERN to the NINO case, Annual-mean sea level pressure (SLP) decreases in the NINO case (relative to the MODERN case) by 10–15 mb in North Pacific, and by 2–4 mb in the North Atlantic (Fig. 1d). Deepening of the Aleutian low in the North Pacific is typical for El Niño events, and has been linked to shifts in storm tracks during El Niño winters (Bjerknes, 1969; Namias and Cayan, 1984). This change in atmospheric circulation is also apparent in the 500 mb geopotential

CPD
7, 199–240, 2011

height anomalies (Fig. 1e) and in the subtropical jet at 200 mb, which intensifies over the central subtropical Pacific by 10–20 m s^{-1}, while relaxing over the northern North Pacific (Fig. 1c). Another striking feature of Fig. 1c is the strong westerly acceleration of winds along the equator, with the zonal-mean zonal wind accelerating by over 20 m/s in the region around the equatorial tropopause (Fig. 3b). As found in past work with imposed equatorial heating perturbations (Hoskins et al., 1999; Inatsu et al., 2002), our NINO case exhibits a state of equatorial superrotation, with upper-level westerlies along the equator.

These changes in the planetary-scale circulation can be interpreted as a response to the imposed shift of warm SSTs into the Central and Eastern Equatorial Pacific, resulting in strong increases in convective precipitation (Fig. 1a and b). The consequent increase in tropospheric heating drives a response similar to the classic Matsuno-Gill solution (Fig. 3a), with planetary-scale Rossby gyres straddling the equator. Such solutions are known to produce superrotation (Showman and Polvani, 2010). However, NINO minus MODERN case differs from the linear Matsuno-Gill solution in that the gyres are shifted east by approximately 1/4 wavelength, so that the upper-level equatorial easterly anomaly coincides with the heating maximum. A similar shift was seen in a simpler model by Kraucunas and Hartmann (2005), who attributed the shift to eastward advection by the strong superrotating mean flow.

The superrotation is itself attributable to momentum convergence onto the equator by the Rossby gyres themselves, particularly the strong, meridionally phase-tilted Pacific gyres. This can be seen by examining the wave activity flux, a standard diagnostic of stationary Rossby wave propagation (Plumb, 1985). Figure 3c shows prominent wave activity flux anomalies emanating from the region of anomalous heating and propagating poleward in both hemispheres, implying a convergence of zonal momentum onto the Equatorial Central Pacific. In the zonal mean (Fig. 3d), this results in an anomalous acceleration of around 4 m s^{-1} day^{-1}, leading to superrotation. Recently, Caballero and Huber (2010) also found a transition to superrotation in warm climate simulations due to equatorial Rossby wave momentum convergence; however, in that case the waves

CPD
7, 199–240, 2011

were transient waves reminiscent of the modern Madden-Julian Oscillation, and thus quite different from the imposed, stationary anomaly of the present study.

The presence of strong, anticyclonic phase-shifted gyres in the subtropical Central Pacific has several consequences. One is the jet anomalies noted in Fig. 1c, which affect the climate of North America (see below). Another is that, because the Matsuno-Gill response corresponds to the first baroclinic mode, the Central Pacific equatorial upper-level easterlies are mirrored by near-surface equatorial westerlies (Fig. 3e). Overall, the Equatorial Pacific response to the permanent El Niño forcing is a reversed Walker cell, with ascent east of the dateline and descent to its west (Fig. 3f). The presence of strong westerly surface wind stress on the equator is consistent with expectations of a permanent El Niño state, and could help stabilize this state in the presence of atmosphere-ocean coupling.

3.3 Regional seasonal temperature and precipitation patterns

Mean annual surface air temperature decreases over most of the continental United States in the NINO case in the high-resolution RegCM3 simulations (Fig. 4a). Temperature decreases over the Southeastern and Southwestern United States in September-October-November (SON), while temperature increases over the Pacific Northwest (Fig. 4b). In addition, negative surface pressure anomalies occur over the east and west coasts, indicating changes in stormtrack direction and intensity in response to the permanent El Niño forcing. Surface air temperature decreases are isolated to the Southeast and Southwest in December-January-February (DJF), with temperatures increasing over the Pacific Northwest (Fig. 4c). Further, large surface pressure anomalies occur over the west and east coasts in DJF (Fig. 4c). Negative temperature anomalies occur over the Southern United States in March-April-May (MAM) (Fig. 4d), and over most of the continental United States in June-July-August (JJA), along with small positive surface pressure anomalies over the Eastern United States (Fig. 4e).

Positive anomalies (NINO minus MODERN) in mean annual precipitation occur over the Southeastern, Western, and Northcentral United States in the high-resolution

CPD
7, 199–240, 2011

RegCM3 simulations (Fig. 5a). Precipitation increases over the east Coast, the Southeast, and California in SON (Fig. 5b), while precipitation increases are isolated to the east Coast, California and parts of the Southwest in DJF. Wind anomalies in DJF suggest increased moisture transport from the sub-tropical Pacific in the NINO case (relative to the MODERN case) (Fig. 5c). Precipitation anomalies are similar in MAM and DJF over most of the United States (Fig. 5d), with the exception of positive anomalies over the Central United States in April, which coincides with the onset of springtime convective precipitation (Castro et al., 2001; Barlow et al., 1998, 2000). Precipitation increases over the Southeast, the Central United States, and the Pacific Northwest in JJA (Fig. 5e). Cyclonic circulation anomalies occur off of the south Atlantic coast in JJA, indicating a change in the summer monsoon circulation in response to the permanent El Niño forcing (see discussion in Sect. 4.2).

3.4 Global and regional seasonal circulation changes

We focus on shifts in boreal winter (DJF), spring (MAM) and summer (JJA) circulation, emphasizing the CAM3 GCM results during DJF (when large-scale features dominate the hydroclimatic response to permanent El Niño-like forcing in the United States), and the RegCM3 nested climate model results during MAM and JJA (when regional-scale features influence the hydroclimatic response).

3.4.1 Large-scale circulation changes

The sub-tropical jet steers synoptic storms in Western North America during DJF especially during El Niño events (Diaz et al., 2001). Following widely-used bandpass filtering approaches (Blackmon et al., 1977, 1980; Chang et al., 2002), we filtered twice-daily atmospheric data over a 2–5 day time period in order to isolate 200 mb transient storm activity during DJF. The CAM3 results show a southward shift in the filtered 200 mb wind fields in the NINO case (relative to MODERN) (Fig. 6a and b), along with an

CPD
7, 199–240, 2011

increase in intensity (Fig. 6a and b) and variance (Fig. 6c).

In addition, transient meridional fluxes are also important for understanding the global energy balance and the intensity of storm tracks (Pierrehumbert, 2002). We analyzed twice-daily atmospheric data in order to calculate transient eddy flux anomalies at 850 mb for heat (VT), water (VQ), and eddy kinetic energy (EKE) over the last 10 model DJFs. The NINO case exhibits increases in meridional water transport over the east and west coasts of the United States and the Central Atlantic, along with decreases over the much of the North Pacific in the vicinity of the Aleutian Low (Fig. 7a). These anomalies in meridional water transport are associated with spatially similar anomalies in meridional heat transport (Fig. 7b) and EKE (Fig. 7c), with the positive anomalies off the coasts of North America also exhibiting increases in annual precipitation in the CAM3 NINO simulation (Fig. 1). The changes in EKE suggest an equatorward shift in the stormtrack in response to the permanent El Niño forcing, with decreases in EKE indicating decreases in storm activity over the Central North Pacific Ocean and increases in EKE indicating increases in storm activity off the coasts of the United States (Fig. 7c).

We used Eady growth rate (Eady, 1949) to quantify the development of baroclinic eddies within the framework of our model results and to help explain the position of the stormtracks presented in earlier sections. The growth rate can be calculated as

$$\sigma = 0.31 f \left[\frac{\partial V}{\partial z} \right] N^{-1}, \quad (1)$$

where N is the Brunt-Vaisala frequency, f is the Coriolis parameter, V is the horizontal wind field and Z is the geopotential height field. The growth rate is computed and averaged over the 600–700 hPa levels (Hoskins and Valdes, 1990). Eady growth rate is a good indicator of storm development because it represents the contributions of both shear and stability. We compute Eady growth rate globally averaged over the last 10 model DJFs and MAMs.

In comparing the NINO and MODERN simulations, Eady growth rate increases over the eastern portion of the Pacific storm track during DJF, while showing little change

CPD
7, 199–240, 2011

over the western portion of the Pacific stormtrack (Fig. 8a and b). This pattern of intensification indicates that the synoptic storms in the Pacific are either intensifying as they move southward over the Central Pacific Ocean or that the entire stormtrack is located further south. The increase in baroclinic instability occurs where latent heat flux (Figure not shown) and precipitation increase (Fig. 5c). In addition, an increases in EKE and baroclinic instability occur during MAM in the Pacific stormtrack (Figure not shown), suggesting that the atmospheric changes in DJF persist into MAM.

3.4.2 Regional-scale circulation changes

The intensification of springtime rainfall is likely to affect precipitation anomalies in the summertime due to soil moisture and upper atmospheric circulation changes. To understand these changes we analyzed data from RegCM3 to see how the seasonal variability of precipitation and soil moisture affects summertime precipitation and temperature.

To show the progression of springtime and summertime precipitation patterns we further decomposed MAM and JJA precipitation anomalies into their monthly components. The March precipitation anomalies (NINO minus MODERN) are spatially similar to the DJF precipitation anomalies, with the largest anomalies occurring over the east and west coasts of the United States (Fig. 9a). The April precipitation anomalies exhibit a similar pattern to the March anomalies, with reductions in the magnitude of the anomalies over the coasts and increases in the magnitude over the Central United States (Fig. 9b). These March and April anomalies indicate winter-like dynamics and a southward shift in the storm track well into the boreal spring. The magnitude of the positive precipitation anomalies over the Central United States persists through August, while the magnitude of the anomalies over the coasts progressively decay each month through the spring and summer (Fig. 9).

CPD
7, 199–240, 2011

The JJA precipitation anomalies in the Midwest and Southeast are partially controlled by a shift in wind direction over the Gulf of Mexico (Fig. 10), with the wind vectors over the Central Gulf Coast land areas that exhibit peak increases in convective precipitation (Fig. 10c) and surface specific humidity (Figure not shown) shifting from southwesterly flow in the MODERN case (Fig. 10b) to southerly-to-southeasterly flow in the NINO case (Fig. 10a). The increases in JJA precipitation over the Central and Southern United States are also associated with decreases in geopotential height and cyclonic circulation anomalies at 500 mb (Fig. 12c).

To isolate changes in available water vapor, we examine the vertically integrated moisture (Q) in the upper atmosphere ~850 mb and above and the lower atmosphere ~850 mb and below. The upper atmospheric moisture is decreased in the NINO case over the Midwestern and Southeast US in June, July, and August (Fig. 11a–c). The upper-level (200 mb) circulation indicates that the sub-tropical jet is intensified in July and August as the mean wind increases over the Rocky Mountains (Figs. 11b,c and 12c). The integrated moisture content between ~850 mb and the surface results in increased moisture availability in the NINO case compared with the MODERN case, indicating enhanced moisture availability in the lower atmosphere in the NINO case. In addition, cyclonic circulation anomalies develop over the Central United States in June, July, and August (Figs. 11d–f; 12c), which should drive increases in summertime precipitation due to enhanced atmospheric instability. The increases in lower level integrated moisture, enhanced cyclonic flow over the eastern half of the United States, and increased sub-tropical jet over the Central United States (Fig. 12c) explain why precipitation is increased over Central United States in response to permanent El Niño forcing.

3.4.3 Secondary soil moisture feedbacks

Previous research has shown that wet springtime months preceding the summertime can lead to an enhanced summertime precipitation (Eltahir, 1998; Findell and Eltahir, 1997, 2003; Pal and Eltahir, 2002). Anomalies between NINO and MODERN show that

CPD
7, 199–240, 2011

surface soil moisture (mm) increases in Pacific Northwest and Midwestern US starting in April and stays elevated throughout JJA (Figure not shown). We will explore the relationship between soil moisture changes and how it affects precipitation anomalies. The hope is that the regional model should be better at resolving the secondary feedbacks not constrained by the global model.

To explore the connection between soil moisture and precipitation we took lag correlations between soil moisture and different atmospheric variables by averaging May through August and lagging precipitation and relative humidity against the May through August average of soil moisture contents (Fig. 13). All correlations will be done using the NINO test case.

We correlate soil moisture to relative humidity to see if increases in soil moisture may induce increases in atmospheric water vapor. Figure 13 shows the correlations between soil moisture (mm) and relative humidity and plots the correlations at lag 0,1,2 where relative humidity lags soil moisture in each case. Lag 0 shows a large correlation between soil moisture and relative humidity across the entire contiguous United States, with largest correlations of 0.8 occurring south of 30° N (Fig. 13c). This pattern is especially seen over the Southeast where soil moisture and relative humidity both increase in the NINO case, but not in the MODERN case (Figure not shown). Next lag correlations are calculated with soil moisture lagging by 1 and 2 months and plotted between (−0.4 and 0.4). At a lag 1 month, soil moisture and relative humidity are positively correlated in the Pacific Northwest and Southeast (Fig. 13b). The correlation of 0.2–0.3 indicates a relationship between soil moisture values in May with increases in relative humidity seen in June (Fig. 13). When relative humidity is lagging by 2 months a positive correlation exists in Pacific Northwest and the Southeast (Fig. 13c), but the correlation begins to diminish and is gone at lag of 3 months. Results show that at a lag of 1 and 2 months that soil moisture values in the Pacific Northwest and Southeast may be related to relative humidity values in June.

In Fig. 13d–f we perform the same analysis except we replace relative humidity with total precipitation $(\text{mm day})^{-1}$. Results for lag 0, show that soil moisture and

CPD
7, 199–240, 2011

precipitation are well correlated. For lag of 1 month and lag of 2 months, correlations between soil moisture and precipitation are spatially similar to the results seen when soil moisture is correlated with relative humidity, except the correlations are reduced. Results from the correlation analysis show that correlation is not extremely strong between soil moisture and precipitation, but a signal still exists over the Southeast and Pacific Northwest. Both of these regions see statistically significant increases in precipitation during JJA and this indicates that the soil moisture feedback may be a secondary feedback in the system, but most likely is not a dominant driver in increasing precipitation due to a permanent El Niño.

4 Discussion

4.1 Pacific storm track changes

We find that permanent El Niño-like forcing drives depression of annual SLP in the North Pacific and intensification of the 200 mb jet, which propagates across the Central Pacific Ocean during DJF and MAM. Stormtracks are intensified during DJF as shown by increases in EKE, moisture and heat transports, and Eady growth rate, consistent with past teleconnection research (Horel and Wallace, 1981; Held et al., 1989; Straus and Shukla, 1997). Decreases in EKE in the North Pacific may indicate less storm activity, but the increases in water and heat transport may indicate more intense storm systems.

Precipitation anomalies over the east and west coasts of the United States during DJF can be explained by a southward shift in stormtracks, resulting in transport of heat and water into more southerly locations (relative to the MODERN simulation). Winter-like atmospheric circulation persists into the spring season over the Pacific, and is associated with increases in baroclinic instability and EKE within the Pacific stormtrack. As the synoptic storms shift southward, increases in intensity may develop because the storms are not cut off from their tropical moisture sources. As a result, the permanent

CPD
7, 199–240, 2011

El Niño forcing produces large increases in precipitation off the west and east coasts of the United States during the winter and into the late spring.

Precipitation anomalies in our results are comparable to modern El Niño events seen via observational studies (Ropelewski and Halpert, 1986; Dai et al., 2000) and El Niño based modeling simulations (Horel and Wallace, 1981). Temperature teleconnections during modern El Niños have varied substantially depending on the El Niño event (Shinker et al., 2009), but in our simulations the DJF temperature teleconnections generally fit the pattern seen in the the observational record (Halpert and Ropelewski, 1992).

4.2 Permanent El Niño and summertime precipitation patterns

We find that permanent El Niño-like forcing increases summertime precipitation in the United States through a number of mechanisms. These mechanisms include (1) shifts in regional circulation that increase moisture availability in the Southeast United States, (2) strengthening of the sub-tropical jet that can control the northward extent of summertime precipitation, and (3) wetter conditions during the springtime that can lead to feedbacks which help to enhance summertime precipitation.

These results compliment previous research trying to describe mechanisms that cause summertime precipitation anomalies (Trenberth and Guillemot, 1996; Pal et al., 2000; Pal and Eltahir, 2002). Summertime precipitation patterns associated with the North American Monsoon (NAM) have been linked to El Niño events (Castro et al., 2001), and a constant ENSO forcing could create a more efficient transfer of heat from the tropics to the mid latitudes due to the development of eddies and movement of Rossby waves affecting stormtracks which can drive the advection of warm moist air from the Gulf of Mexico during JJA (Trenberth et al., 2008; Oort et al., 1996). Our simulations indicate a weaker NAM seen by the development of northeasterly winds over the Great Plains controlled by the low pressure system which develops over the east coast.

CPD
7, 199–240, 2011

However, dynamical connections to ENSO are still uncertain because the warm-season precipitation in the United States is influenced by a number of mechanisms that are potentially sensitive to El Niño forcing. Previous research has shown that the summertime precipitation can shift due geopotential height fluctuations and the development of cyclonic flow over the Midwestern US (Mechoso et al., 2005). Similar studies have shown that summertime precipitation is enhanced due to increased moisture flux from the Gulf of Mexico caused by a displaced intertropical convergence zone (ITCZ) (Mechoso et al., 2005; Higgins and Shi, 2001), or by changes in the subtropical jet, which can effectively pull moisture out of the Gulf of Mexico (Trenberth and Guillemot, 1996). However, the availability of moisture from the Gulf of Mexico is not the only limiting factor in the meridional extent of precipitation during JJA (Chou and Neelin, 2003). For instance, advection of heat from the westerlies also can lead to a reduction of convective JJA monsoonal precipitation (Chou and Neelin, 2003). Other limiting factors controlling the extent of monsoonal precipitation can include ventilation, soil moisture, and the Rodwell-Hoskins Mechanism (IRH) (Chou and Neelin, 2003), which can suppress the convergence zone by inducing subsidence to the west of the monsoon convergence zone. Ultimately, a suite of mechanisms can influence advection of water vapor into the Central United States (Higgins and Shi, 2001). Only some of these processes can be well represented in current global climate models, while others such as IRH may require high-resolution climate models.

In our simulations, summertime precipitation is enhanced due to availability of water vapor that is transported into the Southeast and Midwestern United States due to shifts in large-scale atmospheric circulation and increases in lower-atmospheric moisture. Specifically, the 200 mb jet decreases in intensity above Canada and the Central United States, along with decreases in 200 mb temperature, and EKE. Over the Eastern United States 500 mb geopotential height decreases along with an increase in the subtropical jet over the Rocky mountains (Fig. 12c). Increased availability of moisture is seen as far North as 45° N, indicating that moisture is able to entrain deep into the continental interior because of the movement of the 200 mb jet. In addition, the anomalous

CPD
7, 199–240, 2011

precipitation during the spring helps to create a more efficient environment for summertime precipitation over the Southeast and Pacific Northwest. Together, these processes lead to enhanced precipitation over much of the continental United States during JJA.

When we compare our NINO minus MODERN JJA temperature and precipitation anomalies with the modern El Niño response over North America, our results show a cooler and wetter Southeastern US (Barlow et al., 2000). Interestingly, when the NINO driven anomalies are compared against some CMIP3 El Niño modeling studies the temperature and precipitation patterns seen over North America are spatially similar, but our anomalies are intensified especially for precipitation and temperature (Mo, 2010). This indicates that a permanent El Niño SST distribution may drive different teleconnection patterns during JJA.

4.3 Permanent El Niño and a connection to past and future climate

The Pliocene and Miocene are the most recent intervals of enhanced global warmth and have been inferred from paleoclimate proxies to have been wetter than modern, especially over North America (Axelrod, 1968, 1997; Kurschner et al., 2009; Wolfe, 1994; Pearson and Palmer, 2000; Lyle et al., 2008). Future climate change projections predict the earth to reach the temperature levels of the Pliocene and Miocene, while the future hydroclimatological projections predict an expansion of the sub-tropical dry zones driving aridification over the regions that were wetter during the Pliocene and Miocene (IPCC, 2007). This creates an apparent contradiction between paleoclimate proxies and future hydroclimate predictions.

However, changes in the ocean and the associated atmospheric interactions could also explain higher mid-latitude temperatures and wetter conditions (Lyle et al., 2008; Vizcaino et al., 2010). Specifically, a permanent El Niño or increased El Niño frequency during the Pliocene and Miocene could have caused conditions to be warmer over Alaska and Canada and wetter in the Western United States. Our results suggest that permanent El Niño-like forcing would have increased high-latitude warming over Alaska and Canada between 2–5 K, while also increasing precipitation over the

CPD
7, 199–240, 2011

continental United States for most of the year by forcing shifts in the global and regional atmospheric circulation.

A number of recent studies have explored mechanisms capable of sustaining a permanent El Niños in climate models (Fedorov et al., 2010; Sriver and Huber, 2010). These studies have shown that increased tropical cyclone ocean mixing can push the East Equatorial Pacific into a more El Niño-like state as a result of sub-tropical ocean mixing that allows warmer water parcels to resurface at the equator (Fedorov et al., 2010; Sriver and Huber, 2010). These modeling studies give a plausible physical mechanism for the permanent El Niño and expanded warm pool in the Eastern Equatorial Pacific that has been inferred from Pliocene proxy records (Ravelo et al., 2004; Brierley et al., 2009).

Other work has suggested that a transition to superrotation could lead to a permanent El Niño state through weakening of the trade winds (Pierrehumbert, 2000; Tziperman and Farrell, 2009). Our experiments have shown that the presence of a strong, persistent El Niño anomaly causes superrotation and actually leads to a reversal of the trade winds, i.e. to surface westerlies along the Equatorial Pacific. This constitutes a potential positive feedback loop that could produce a stable, large-amplitude permanent El Niño state. Further investigation of this supperrotation hypothesis will require additional experiments with fully-coupled ocean-atmosphere climate models.

5 Conclusions

We have used high-resolution global and nested climate models to explore the possible atmospheric dynamics that could develop if ENSO were to deviate towards a permanent El Niño-like state. Our results generally agree with the hydrologic cycle blueprint presented by Molnar and Cane (2002), and with present El Niño teleconnections. Global precipitation anomalies driven by a permanent El Niño result in mean annual precipitation anomalies throughout the tropics and the monsoon regions, including increases of 40–70 cm year^{-1} over the continental United States. During DJF,

CPD
7, 199–240, 2011

the Aleutian low deepens, and the 200 mb jet intensifies and shifts southward. During MAM, the Pacific stormtrack intensifies due to increases in EKE and Eady growth. During JJA, precipitation increases are associated with shifts in the upper atmospheric jet and increased atmospheric moisture availability, while feedbacks from spring soil moisture to summer precipitation are relatively weak. This shift in JJA circulation does not seem to be associated to an intensification of NAM and leads to large scale increases in precipitation over the entire Eastern United States. Further, our experiments indicate that persistent El Niño-like conditions could result in supperrotation and a reversal of the trade winds, a mechanism that could help to explain past periods in which climate proxies suggest a permanent El Niño state.

Acknowledgements. Thank you to Ki-Hong Min, Michael Alexander, and Ruben van Hooidonk for their helpful suggestions during preparation of this manuscript. Thank you to the Computational Sciences and Engineering (CS&E) program which supports the first author through a GAANN fellowship. In addition, parts of this research were funded by NSF grants, EAR-0450221 and OCE-0902882.

References

Ashfaq, M., Shi, Y., Tung, W.-W., Trapp, R. J., Gao, X., Pal, J. S. and Diffenbaugh, N. S.: Suppression of South Asian summer monsoon precipitation in the 21st century, Geophys. Res. Lett., 36, L01704, doi:10.1029/2008GL036500, 2009. 206

Axelrod, D. I.: Tertiary floras and topographic history of the Snake River Basin, Idaho, Bull. Geol. Soc. Am., 79, 713–733, 1968. 218

Axelrod, D. I.: Outline history of California vegetation, in: Terrestrial Vegetation of California, edited by: Barbour, M. and Major, J., New York, John Wiley and Sons, 139–193, 1997. 201, 218

Barlow, M., Nigam, S., and Berber, E. H.: ENSO, Pacific decadal variability, and US summertime precipitation, drought, and streamow, J. Climate, 14, 2105–2128, 2000. 218

Barreiro, M., Philander, G., Pacanowski, R., and Fedorov, A.: Simulations of warm tropical conditions with application to middle Pliocene atmospheres, Clim. Dynam., 26, 349–365, 2006.

Bjerknes, J.: Atmospheric teleconnections from the Equatorial Pacific, Mon. Weather Rev., 97, 163–172, 1969. 207
Blackmon, M. L. and Lau, N. C.: Regional characteristics of the Northern Hemisphere wintertime circulation: a comparison of the simulation of a gfdl general circulation model with observations, J. Atmos. Sci., 37, 497–514, 1980. 210
Blackmon, M. L., Wallace, J. M., Lau, N. C., and Mullen, S. L.: An observational study of the Northern Hemisphere wintertime circulation, J. Atmos. Sci., 34, 1040–1053, 1977. 210
Brierley, C. M., Fedorov, A. V., Liu, Z., Herbert, T. D., and Lawrence, K. T., and La Riviere, J. P.: Greatly expanded tropical warm pool and weakened hadley circulation in the early pliocene, Science, 323, 1714–1718, 2009. 202, 219
Caballero, R. and Huberm, M.: Spontaneous transition to superrotation in warm climates simulated by CAM3, Geophys. Res. Lett., 37, L11701, doi:10.1029/2010GL043468, 2010.
Castro, C. L., McKee, T. B., and Pielke Sr, R. A.: The relationship of the North American Monsoon to Tropical and North Pacific Sea surface temperatures as revealed by observational analyses, J. Climate, 14, 4449–4473, 2001. 203
Cerling, T. E., Harris, J. M., MacFadden, B. J., Leakey, M. G., Quade, J., Eisenmann, V., and Ehleringer, J. R.: Global vegetation change through the Miocene/Pliocene boundary, Nature, 389, 153–158, 1997. 201
Chang, E. K. M., Lee, S., and Swanson, K. L.: Storm track dynamics, J. Climate, 15, 2163–2183, 2002. 210
Chiang, J. C. H.: The tropics in paleoclimate, Annu. Rev. Earth. Pl. Sc., 37, 263–297, 2009. 201
Chou, C. and Neelin, J. D.: Limiting the northward extent of the northern summer monsoons over North America, Asia, South America, J. Climate, 66, 442–425, 2003. 217
Cole, J. E., Overpeck, J. T., and Cook, E. R.: Multiyear La Nina events and persistent drought in the contiguous United States, Geophys. Res. Lett., 29(13), 1647, doi:10.1029/2001GL013561, 2002. 201
Collins, W. D., Bitz, C. M., Blackmon, M. L., and Bonan, G. B.: The Community Climate System Model: CCSM3, J. Climate, 19, 212–214, 2006. 204
Cook, E. R., Woodhouse, C. A., Eakin, C. M., Meko, D. M., and Stahle, D. W.: Long-term aridity changes in the Western United States, Science, 306(5698), 1015–1018, 2004. 201
Crowley, T. J.: Pliocene climates: the nature of the problem, Mar. Micropaleontol., 27, 3–12, 1996. 201

CPD
7, 199–240, 2011

Dai, A. and Wigley, T. M. L.: Global patterns of ENSO-induced precipitation, Geophys. Res. Lett., 27(9), 1283–1286, 2000. 216
Diaz, H. F., Hoerling, M. P., and Eischeid, J. K.: ENSO variability, teleconnections and climate change, Int. J. Climatol., 21, 1845–1862, 2001. 206, 210
Diffenbaugh, N. S. and Ashfaq, M.: Intensification of hot extremes in the United States, Geophys. Res. Lett., 37, L15701, doi:10.1029.GL043888, 2010. 203, 205
Diffenbaugh, N. S., Pal, J. S., Trapp, R. J., and Giorgi, F.: Fine-scale processes regulate the response of extreme events to global climate change, P. Natl. Acad. Sci., 102(44), 15774–15778, 2005. 203, 206
Diffenbaugh, N. S., Ashfaq, M., Shuman, B., Williams, J. W., and Bartlein, P. J.: Summer aridity in the United States: response to mid-Holocene changes in insolation and sea surface temperature, Geophys. Res. Lett., 33, L22712, doi:10.1029/2006GL028012, 2006. 205
Dekens, P. S., Ravelo, A. C., and McCarthy, M.: Warm upwelling regions in the warm Pliocene, Paleoceanography, 22, doi:10.1029/2006PA001394, 2007. 202
Dekens, P. S., Ravelo, A. C., McCarthy, M. D., and Edwards, C. A.: A 5 million year comparison of Mg/Ca and alkenone paleo-thermometers, G3, 9, Q10001, doi:10.1029/2007GC001931, 2008. 202, 204
Eady, E. T.: Long waves and cyclone waves, Tellus, 1, 33–52, 1949. 211
Eltahir, E. A.: A soil moisture-rainfall feedback mechanism, 1. Theory and observations, Water Resour. Res., 34, 765–776, 1998. 213
Fedorov, A. and Philander, G.: Is El Niño changing?, Science, 288, 1977–2002, 2000. 201
Fedorov, A. V., Dekens, P. S., McCarthy, M., Ravelo, A. C., deMenocal, P. B., Barreiro, M., Pacanowski, R. C., and Philander, S. G.: The Pliocene paradox (Mechanisms for a permanent El Niño), Science, 312, 1485–1489, 2006. 202
Fedorov, A. V., Brierley, C. M., and Emanuel, K.: Tropical cyclones and permanent El Niño in the early pliocene epoch, Nature, 463(7284), 1066–1070, 2010. 219
Findell, K. L. and Eltahir, E. A.: An analysis of the soil moisture rainfall feedback, based on direct obser vations from Illinois, Water Resour. Res., 33, 725–735, 1997. 213
Findell, K. L. and Eltahir, E. A. B.: Atmospheric controls on soil moisture-boundary layer interactions, Part Feedbacks within the Continental United States, J. Hydrometeorol., 4, 570–583, 2003. 213
Fortelius, M., Eronen, J., Jernvall, J., Liu, L., Pushkina, D., Rinne, J., Tesakov, A., Vislobokova, I., Zhang, Z., Zhou, L.: Fossil mammals resolve regional patterns of Eurasian

CPD
7, 199–240, 2011

climate change during 20 million years, Evol. Ecol. Res., 4, 1005–1016, 2002. 201
Hack, J. J., Caron, J. M., Yeager, S. G., Oleson, K. W., Holland, M. M., Truesdale, J. E., and Rasch, P. J.: Simulation of the global hydrological cycle in the CCSM community atmosphere model version 3 (Cam3): mean features, J. Climate, 19, 2199–2221, 2006. 204
Halpert, M. S. and Ropelewski, C. F.: Surface temperature patterns associated with the Southern Oscillation, J. Climate, 5, 577–593, 1992. 216
Haywood, A. M. and Valdes, P. J.: Modelling middle Pliocene warmth: contribution of atmosphere, oceans and cryosphere, Earth Planet Sc. Lett., 218, 363–377, 2004. 205
Held, I. M. and Soden, B. J.: Robust responses of the hydrological cycle to global warming, J. Climate, 19, 5686–5699, 2006. 201, 207
Held, I. M., Lyons, S. W., and Nigam, S.: Transients and the extratropical response to El Niño, J. Atmos. Sci., 46, 163–174, 1989. 215
Herold, N., Seton, M., Mueller, R. D., You, Y., and Huber, M.: Middle Miocene tectonic boundary conditions for use in climate models, Geochem. Geophy. Geosy., 9, Q10009, doi: 10.1029/2008GC002046, 2008. 205
Higgins, R. W. and Shi, W.: Intercomparison of the principal modes of interannual and intraseasonal variability of the North American monsoon system, J. Climate, 14, 403–417, 2001. 217
Horel, J. D. and Wallace, J. M.: Planetary-scale atmospheric phenomena associated with the Southern Oscillation, Mon. Weather Rev., 109, 813–829, 1981. 203, 215, 216
Hoskins, B. J. and Valdes, P. J.: On the existence of storm tracks, J. Atmos. Sci., 47, 1854–1864, 1990. 211
Hoskins, B., Neale, R., Rodwell, M., and Yang, G.: Aspects of the large-scale tropical atmospheric circulation, Tellus A, 51, 33–44, 1999. 208
Huang, Y., Clemens, S. C., Liu, W., Wang, Y., and Prell, W. L.: Large-scale hydrological change drove the late Miocene C4 plant expansion in the Himalayan foreland and Arabian Peninsula, Geology, 35, 531–534, 2007. 201
Huffman, G. J, Adler, R. F, Arkin, P. A, Chang, A., Ferraro, R., Gruber, A., Janowiak, J., McNab, A., Rudolf, B., and Schneider, U.: The Global Precipitation Climatology Project (GPCP) combined precipitation dataset, B. Am. Meteorol. Soc., 78, 5–20, 1997. 207
Hurrell, J. W. and Trenberth, K. E.: Global sea surface temperature analyses: multiple problems and their implications for climate analysis, modeling, and reanalysis, B. Am. Meteorol. Soc., 80, 2661–2678, 1999. 204

CPD
7, 199–240, 2011

Hurrell, J. W., Hack, J. J., Phillips, A. S., Caron, J., and Yin, J.: The dynamical simulation of the community atmosphere model version 3 (CAM3), J. Climate, 19, 2162–2183, 2006. 204
Huybers, P. and Molnar, P.: Tropical cooling and the onset of North American glaciation, Clim. Past, 3, 549–557, doi:10.5194/cp-3-549-2007, 2007.
Inatsu, M., Mukougawa, H., and Xie, S.: Stationary eddy response to surface boundary forcing: idealized GCM experiments, J. Atmos. Sci., 59, 1898–1915, 2002. 208
Joseph, R. and Nigam, S.: ENSO evolution and teleconnections in IPCCs 20th century climate simulations: realistic representation?, J. Climate, 19, 4360–4377, 2006. 204
Karnauskas, K., Seager, R., Kaplan, A., Kushnir, Y., and Cane, M. A.: Observed strengthening of the zonal sea surface temperature gradient across the Equatorial Pacific Ocean, J. Climate, 22, 4316–4321, 2009. 202
Kraucunas, I. and Hartmann, D.: Equatorial superrotation and the factors controlling the zonal-mean zonal winds in the tropical upper troposphere, J. Atmos. Sci., 62, 371–389, 2005.
Kurschner, W. M., Kvacek, Z., and Dilcher, D.: The impact of Miocene atmospheric carbon dioxide fluctuations on climate and the evolution of terrestrial ecosystems, P. Natl. Acad. Sci. USA, 105, 449–453, 2009. 201, 218
Lyle, M., Barron, J., Bralower J., Huber, M, Lyle, A. O., Ravelo, A. C., Rea, R. K., and Wilson, P.: Pacific Ocean and cenozoic evolution of climate, Rev. Geophys., 46, RG2002, doi:10.1029/2005RG000190, 2008. 201, 218
Mechoso, C. R., Robertson, A. W., Ropelewski, C. F., and Grimm, A. M.: The American Monsoon Systems: an Introduction. The Global Monsoon System: Research and Forecast, edited by: Chang, C. P., Wang, B., and Lau, N. C. G., WMO/TD No. 1266 (TMRP Report No. 70), 197–206, 2005. 217
Meehl, G., Arblaster, J., Lawrence, D., Seth, A., Schneider, E., and Kirtman, B.: Monsoon regimes in the CCSM3, J. Climate, 19(11), 2482–2495, 2006. 204
Mo, K. C.: Interdecadal modulation of the impact of ENSO on precipitation and temperature over the United States, J. Climate, 23(13), 3639–3656, 2010. 218
Molnar, P. and Cane, M. A.: El Niño's tropical climate and teleconnections as a blueprint for pre-Ice Age climates, Paleoceanography, 17(2), 1021, doi:10.1029/2001PA000663, 2002. 207
Molnar, P. and Cane, M. A.: Early Pliocene (pre–Ice Age) El Niño like global climate: which El Niño?, Geosphere, 3, 337–365, 2007.
Namias, J. and Cayan, D. R.: El Niño: implications for forecasting, Oceanus 27, 41–47, 1984.

CPD
7, 199–240, 2011

207
O'Gorman, P. and Schneider, T.: Precipitation extreme changes exceeding moisture content increases in MIROC and IPCC climate models, P. Natl. Acad. Sci., 107(2), 571–575, 2010. 201
Oort, A. H. and Yienger, J. J.: Observed interannual variability in the hadley circulation and its connection to enso, J. Climate, 9, 2751–2767, 1996. 216
Pagani, M., Arthur, M. A., and Freeman, K. H.: Miocene evolution of atmospheric carbon dioxide, Paleoceanography, 14, 273–292, 1999. 201
Pal, J. S. and Eltahir, E. A.: Pathways relating soil moisture conditions to future summer rainfall within the land-atmosphere system, J. Climate, 15, 1227–1242, 2000.
Pal, J. S. and Eltahir, E. A.: Teleconnections of soil moisture and rainfall during the 1993 midwest summer flood, Geophys. Res. Lett., 29(18), 1865, doi:10.1029/2002GL014815, 2002. 213, 216
Pal, J. S., Eltahir, E. A., and Small, E. E.: Simulation of regional-scale water and energy budgets – representation of subgrid cloud and precipitation processes within RegCM, J. Geophys. Res., 105(D24), 29579–29594, doi:10.1029/2000JD900415, 2000. 216
Pal, J. S., Giorgi, F., Bi, X., Elguindi, N., and Solmon, F.: Regional climate modeling for the developing world: the Ictp Regcm3 and Regcnet, B. Am. Meteorol. Soc., 88(9), p. 1395, 2007. 205
Pearson, P. N. and Palmer, M. R.: Atmospheric carbon dioxide concentrations over the past 60 million years, Nature, 406, 695–699, 2000. 201, 218
Pierrehumbert, R. T.: Climate change and the Tropical Pacific: the sleeping dragon wakes, P. Natl. Acad. Sci., 97, 1355–1358, 2000. 219
Pierrehumbert, R. T.: The hydrologic cycle in deep time climate problems, Nature 419, 191–198, 2002. 201, 211
Plumb, R.: On the three-dimensional propagation of stationary waves, J. Atmos. Sci., 42, 217–229, 1985. 208
Rauscher, S. A., Pal, J. S., and Diffenbaugh, N. S.: Future changes in snowmelt-driven runoff timing over the Western US, Geophys. Res. Lett., 35, L16703, doi:10.1029/2008GL034424, 2008. 205, 206
Ravelo, A. C., Andreasen, D. H., Lyle, M., Lyle, A. O., and Wara, M. W.: Regional climate shifts caused by gradual global cooling in the Pliocene epoch, Nature, 429, 263–267, 2004. 201, 202, 219

CPD
7, 199–240, 2011

Raymo, M. E., Grant, B., Horowitz, M., and Rau, G. H.: Mid-Pliocene warmth: stronger greenhouse and stronger conveyor, Mar. Micropaleontol., 27, 313–326, 1996. 201
Ropelewski, C. F. and Halpert, M. S.: North American precipitation and temperature patterns associated with the El Niño/Southern Oscillation (ENSO), Mon. Weather Rev., 114, 2352–2362, 1986. 216
Sang-Wook Y., Jong-Seong, K., Boris, D., Min-Ho, K., Kirtman, B. P., and Fei-Fei, J.: El Niño in a changing climate, Nature, 461(7263), 511–514, 2009. 202
Seager, R. and Vecchi, G. A.: Greenhouse warming and the 21st Century hydroclimate of southwestern North America, P. Natl. Acad. Sci. USA, doi: 10.1073/pnas.0910856107, 2010. 201
Seager, R., Ting, M., Held, I., Kushnir, Y., Lu, J., Vecchi, G., Huang, H. P., Harnik, N., Leetmaa, A., and Lau, N. C.: Model projections of an imminent transition to a more arid climate in Southwestern North America, Science, 316, 1181–1184, 2007. 201
Shinker, J. and Bartlein, P. J.: Visualizing the large-scale patterns of ENSO-related climate anomalies in North America, Earth Interact., 13(3), 1–50, 2009. 216
Showman, A. P. and Polvani, L. M.: The Matsuno-Gill model and equatorial superrotation, Geophys. Res. Lett., 37, L18811, doi:10.1029/2010GL044343, 2010. 208
Shukla, S. P., Chandler, M. A., Jonas, J., Sohl, L. E., Mankoff, K., and Dowsett, H.: Impact of a permanent El Niño (El Padre) and Indian Ocean dipole in warm Pliocene climates, Paleoceanography, 24, PA2221, doi:10.1029/2008PA001682, 2009.
Sriver, L. and Huber, M.: Modeled sensitivity of upper thermocline properties to tropical cyclone winds and possible feedbacks on the hadley circulation, Geophys. Res. Lett., 37(8), L08704, 2010. 219
Straus, D. M. and Shukla, J.: Variations of midlatitude transient dynamics associated with ENSO, J. Atmos. Sci., 54, 777–790, 1997. 215
Trapp, R. J., Diffenbaugh, N. S., Brooks, H. E., Baldwin, M. E., Robinson, E. D., and Pal, J. S.: Changes in severe thunderstorm environment frequency during the 21st century caused by anthropogenically enhanced global radiative forcing, P. Natl. Acad. Sci. USA, 104(50), 19719–19723, 2007. 206
Trenberth, K. E. and Guillemot, J.: Physical processes involved in the 1988 drought and 1993 flood in North America, J. Climate, 9, 1288–1298, 1996. 216, 217
Trenberth, K. E. and Hoar, T. J.: El Niño and climate change, Geophys. Res. Lett., 24, 3057–3060, 1997. 206

CPD
7, 199–240, 2011

Trenberth, K. E. and Hurrell, J. W.: Decadal atmosphere-ocean variations in the Pacific, Clim. Dynam., 9, 303–319, 1994.
Trenberth, K. E., Branstator, G. W., Karoly, D., Kumar, A., Lau, N. C., and Ropelewski, C.: Progress during toga in understanding and modeling global teleconnections associated with tropical sea surface temperatures, J. Geophys. Res., 103(14), 291–324, 1998. 203, 216
Tziperman, E. and Farrell, B. F.: The pliocene equatorial temperature lessons from atmospheric superrotation, Paleoceanography, 24, PA1101, doi:10.1029/2008PA001652, 2009. 219
Vizcaino, M., Rupper, S., and Chiang, J. C. H.: Permanent El Niño and the onset of Northern Hemisphere glaciations: mechanism and comparison with other hypotheses, Paleoceanography, revised, 2010. 218
Walker, M. D. and Diffenbaugh, N. S.: Evaluation of high-resolution simulations of daily-scale temperature and precipitation over the United States, Clim. Dynam., doi:10.1007/s00382-009-0603-y, 2009. 205
Wara, M. W., Ravelo, A. C., and Delaney, M. L.: Permanent El Niño-like conditions during the Pliocene warm period, Science, 309(5735), 758–761, 2005. 202, 204
Wolfe, J. A.: Tertiary climatic changes at middle latitudes of Western North America, Palaeogeogr. Palaeocl., 108, 195–205, 1994. 201, 218
Xie, P. and Arkin, P. A.: Global precipitation: a 17-year monthly analysis based on gauge obser vations, satellite estimates, and numerical model outputs, B. Am. Meteorol. Soc., 78, 2539–2558, 1997. 207
You, Y., Huber, M., Mueller, D., Poulsen, C. J., and Ribbe, J.: Simulation of the Middle Miocene climate optimum, Geophys. Res. Lett., 36, L04702, doi:10.1029/2008GL036571, 2009. 205
Zachos, J., Pagani, M., Sloan, L., Thomas, E., and Billups, K.: Trends, rhythms and aberrations in global climate 65 Ma to present, Science, 292, 686–693, 2001. 201

CPD
7, 199–240, 2011

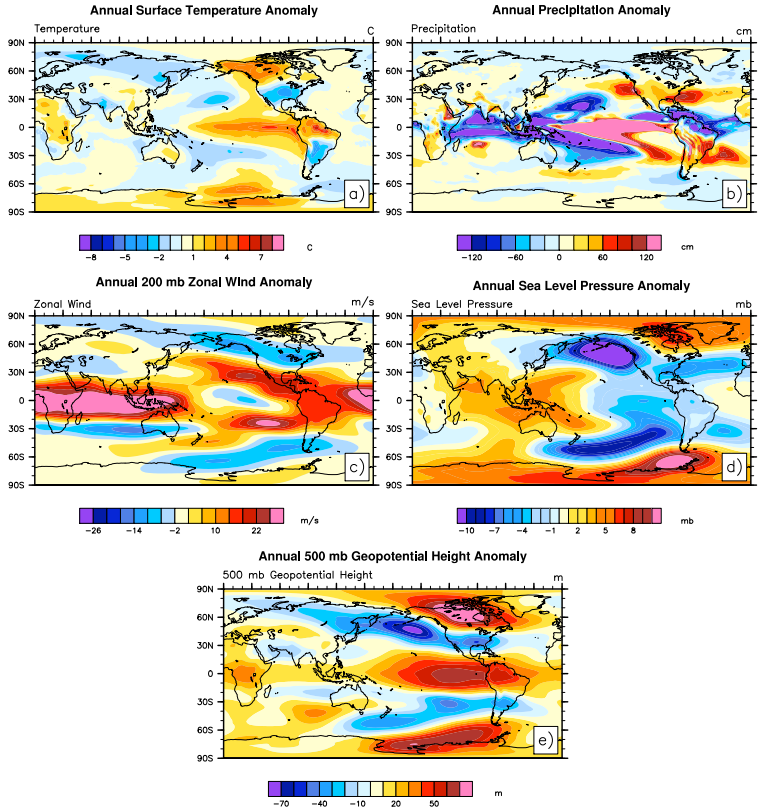

Fig. 1. Figure 1 shows the mean annual anomalies between the NINO and MODERN case for basic atmospheric variables. Surface temperature anomalies between NINO case and MODERN case in °C **(a)**. Mean annual cumulative precipitation anomaly between NINO and MODERN in cm year^{-1} **(b)**. Zonal wind anomaly interpolated at the 200 mb pressure level in m s^{-1} **(c)**. Sea level pressure anomaly between NINO case and MODERN case in mb **(d)**. Geopotential height anomaly between NINO case and MODERN case in meters **(e)**.

CPD
7, 199–240, 2011

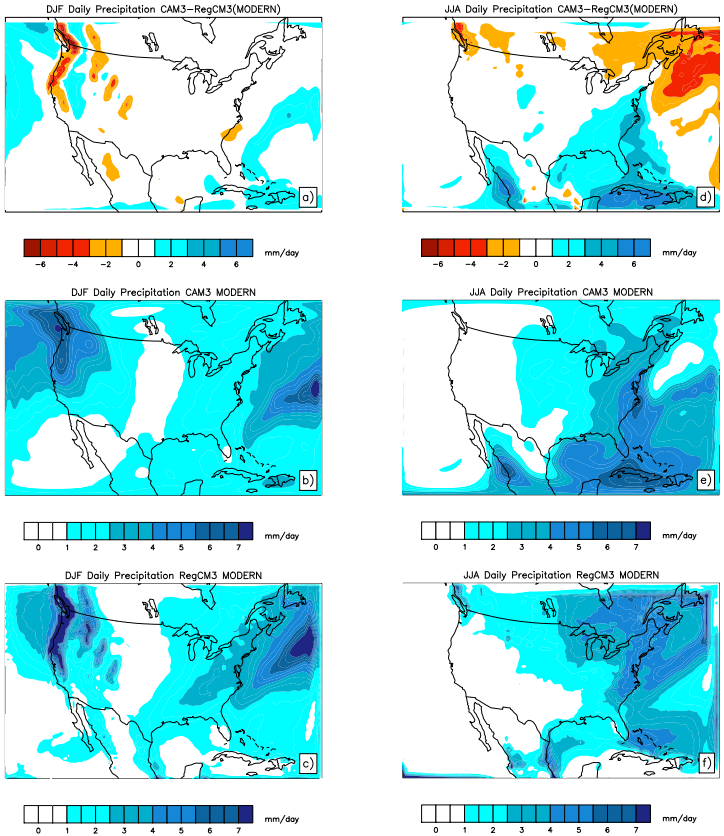

Fig. 2. CAM3.0 T85 MODERN DJF precipitation (mm day^{-1}) comparison to RegCM3 MODERN DJF precipitation (mm day^{-1}) **(a)**, CAM3.0 T85 MODERN DJF precipitation **(b)**, RegCM3 MODERN DJF precipitation **(c)**. CAM3.0 T85 MODERN JJA precipitation (mm day^{-1}) comparison to RegCM3 MODERN JJA precipitation (mm day^{-1}) **(d)**, CAM3.0 T85 MODERN JJA precipitation **(e)**, RegCM3 MODERN JJA precipitation **(f)**.

CPD
7, 199–240, 2011

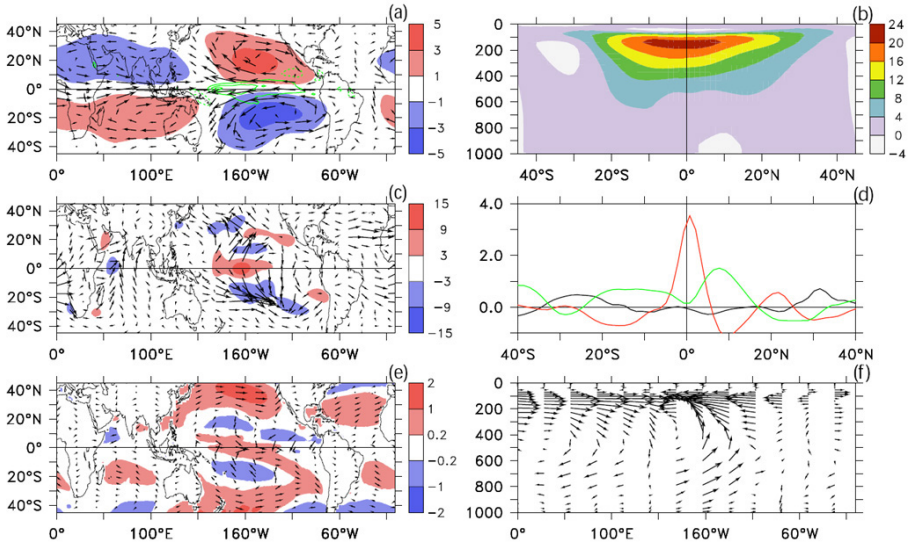

Fig. 3. Annual-mean climatological NINO–MODERN anomalies in the tropical region. **(a)** Eddy streamfunction (shading, units of $10^7\,m^2\,s^{-1}$) and wind (arrows, longest about $30\,m\,s^{-1}$) averaged over 100–200 hPa, and convective precipitation rate (green contours at intervals of $10\,mm\,day^{-1}$, negative dashed). **(b)** Zonal-mean zonal wind ($m\,s^{-1}$). **(c)** Stationary wave activity flux (arrows, longest about $100\,m^2\,s^{-2}$) and its convergence (shading, units of $m\,s^{-1}\,day^{-1}$), averaged over 100–200 hPa. **(d)** Zonal-mean zonal momentum tendency (units of $m\,s^{-1}\,day^{-1}$) averaged over 100–200 hPa due to mean vorticity flux $(f+\overline{\zeta})\overline{v}$ (green), stationary eddy momentum flux convergence (red) and transient eddy momentum flux convergence (black). **(e)** Horizontal wind in the lowest model layer (arrows, longest about $8\,m\,s^{-1}$) and zonal component of surface wind stress over ocean (shading, units of $0.1\,N\,m^2$). **(f)** Zonal-vertical wind in the equatorial region, averaged 5° S–5° N. Vertical (pressure) velocity component has been multiplied by −100 for display purposes.

CPD
7, 199–240, 2011

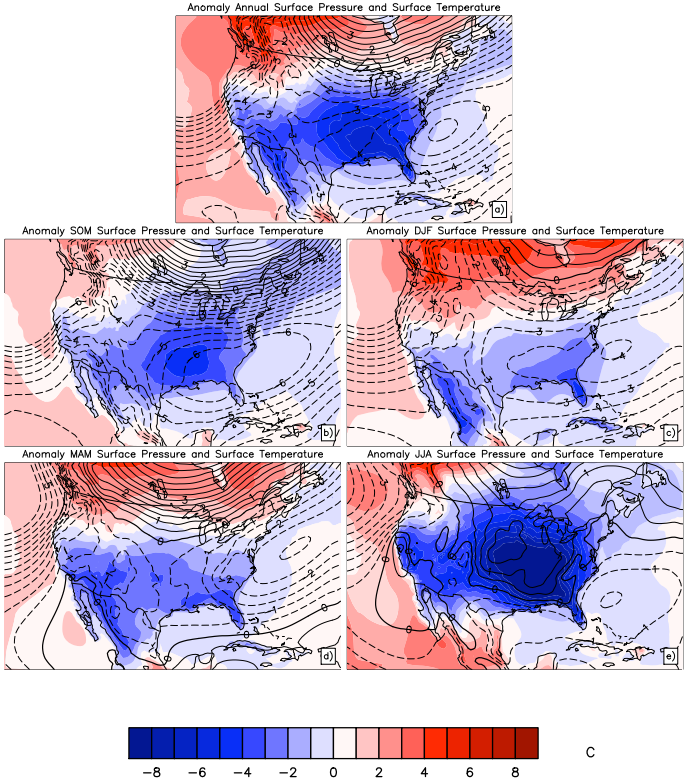

Fig. 4. Temperature anomalies (°C) for NINO minus MODERN from RegCM3 results. Mean annual anomaly **(a)**, September, October, November (SOM) anomaly **(b)**, December, January, February (DJF) anomaly **(c)**, March, April, May anomaly **(d)**, June, July, August anomaly **(e)**. Contour lines represent pressure anomalies in mb, where negative values are dashed, positive values are constant, and thick black line is the zero contour.

CPD
7, 199–240, 2011

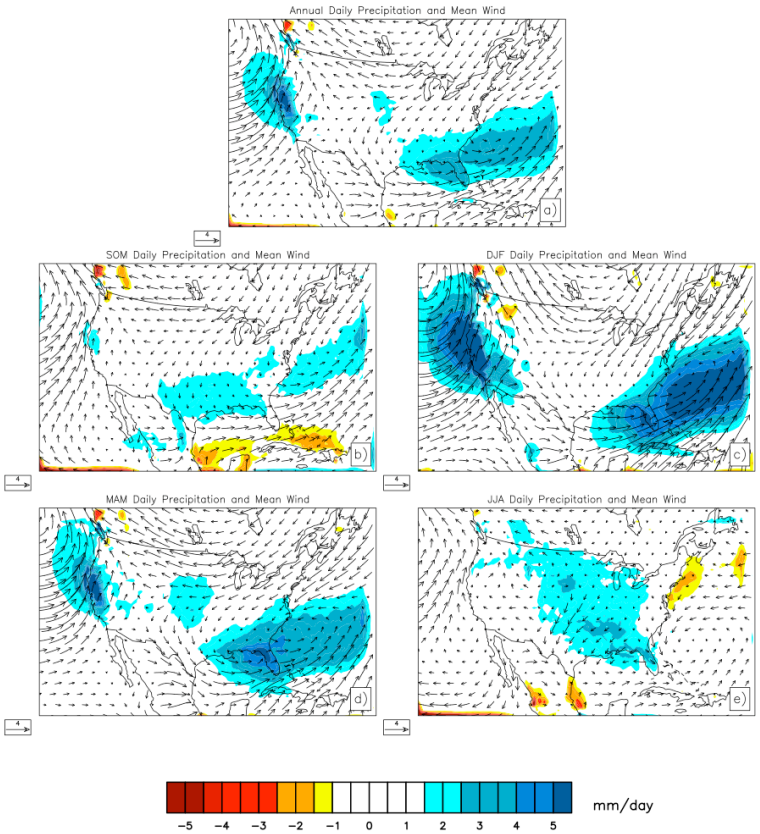

Fig. 5. Precipitation anomalies (mm day^{-1}) for NINO minus MODERN from RegCM3. Mean annual anomaly **(a)**, SOM precipitation anomalies **(a)**, DJF precipitation anomalies **(c)**, MAM precipitation anomalies **(d)**, and JJA precipitation anomalies **(e)**. Vectors are placed over the precipitation contours and represent mean wind (m s^{-1}) at lowest model level.

CPD
7, 199–240, 2011

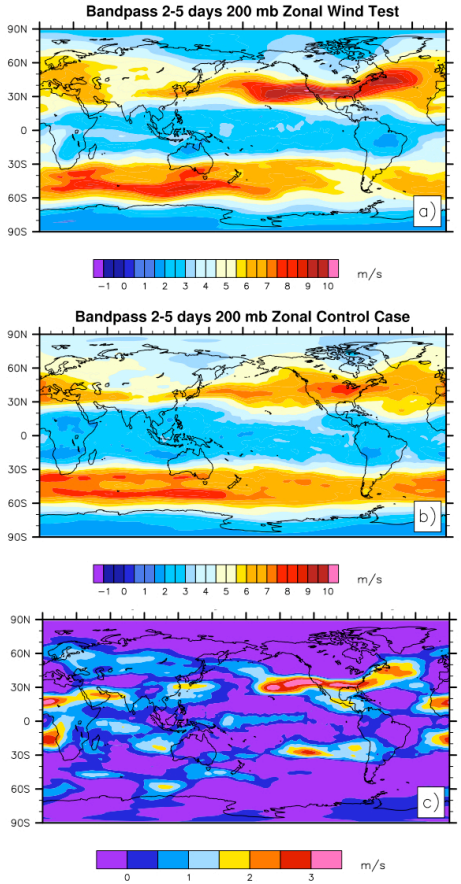

Fig. 6. Bandpass Blackmon filtering (2–5 days) for zonal wind at 200 mb. The NINO case **(a)**, MODERN case **(b)**, and difference between NINO and MODERN **(c)** in m s^{-1}.

CPD
7, 199–240, 2011

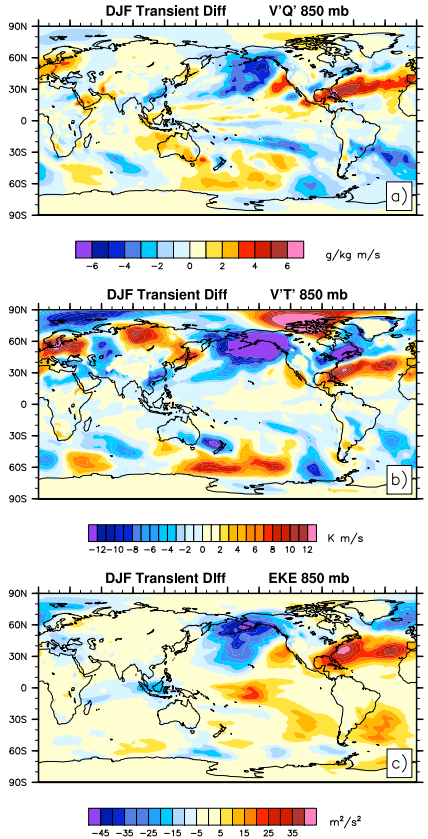

Fig. 7. 2X daily data analyzed using eddy flux calculations: equation $x'y'=\text{ave}(x{\cdot}y)-X{\cdot}Y$. Meridional water transport **(a)** in g/kg m s^{-1}, meridional heat transport K m s^{-1} **(b)**, and eddy kinetic energy m^2 s^{-2} (EKE) **(c)** averaged over averaged over the last ten model Winters (DJF) for NINO minus MODERN.

CPD
7, 199–240, 2011

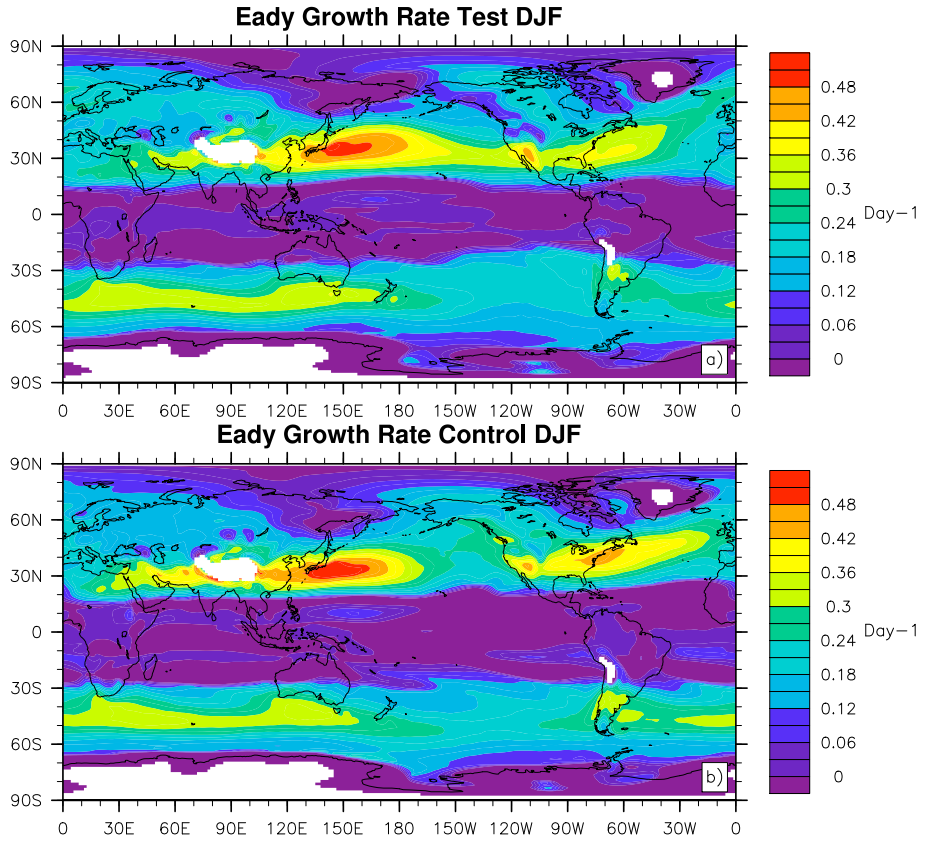

Fig. 8. Eady growth rate (computed as in Hoskins and Valdes, 1990) for the DJF NINO case **(a)**, and DJF MODERN case **(b)** units are day^{-1}. See Sect. 3.4.1.

CPD
7, 199–240, 2011

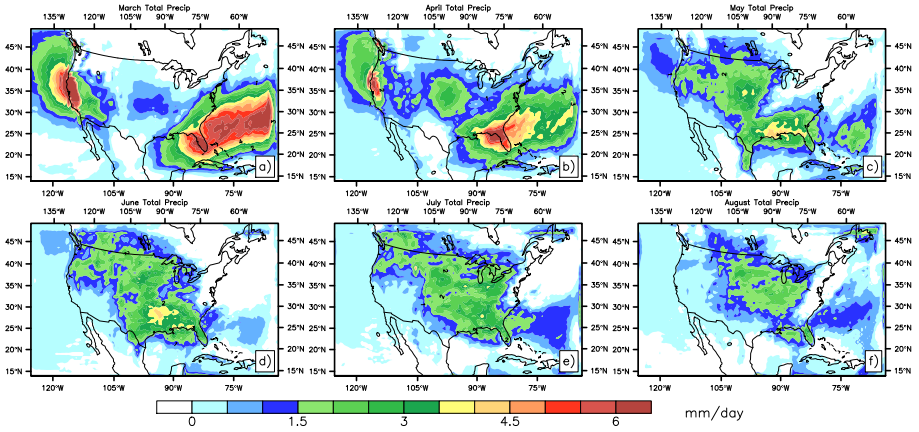

Fig. 9. Decomposed anomalous monthly precipitation results (mm day^{-1}) for MAM and JJA for NINO minus MODERN from RegCM3. Plots are March **(a)**, April **(b)**, May **(c)**. Plots for June **(d)**, July **(e)**, August **(f)**.

CPD
7, 199–240, 2011

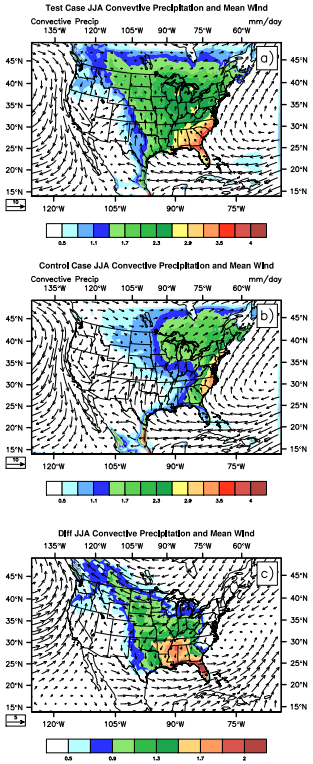

Fig. 10. JJA mean wind (U,V) in m s^{-1} plotted as vectors and convective precipitation mm day^{-1} as the contour. NINO minus MODERN **(a)**, NINO case **(b)**, and MODERN case **(c)**.

CPD
7, 199–240, 2011

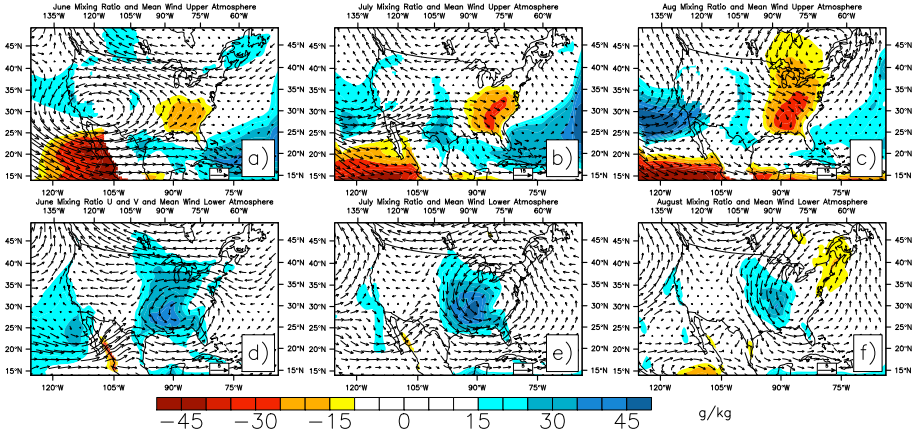

Fig. 11. Is NINO minus MODERN total column integrated moisture content subtracted from lower (~850 to surface) integrated moisture isolating moisture content in the upper atmosphere (g/kg). Upper integrated moisture for June **(a)**, July **(b)**, August **(c)**, with the vectors representing mean wind ($m\,s^{-1}$) anomaly between NINO and MODERN plotted at model level 3 (~200 mb). Lower integrated moisture content (~850 to surface) for June **(d)**, July **(e)**, August **(f)** between NINO and MODERN. Mean wind is plotted at model level 16 (~850 mb).

CPD
7, 199–240, 2011

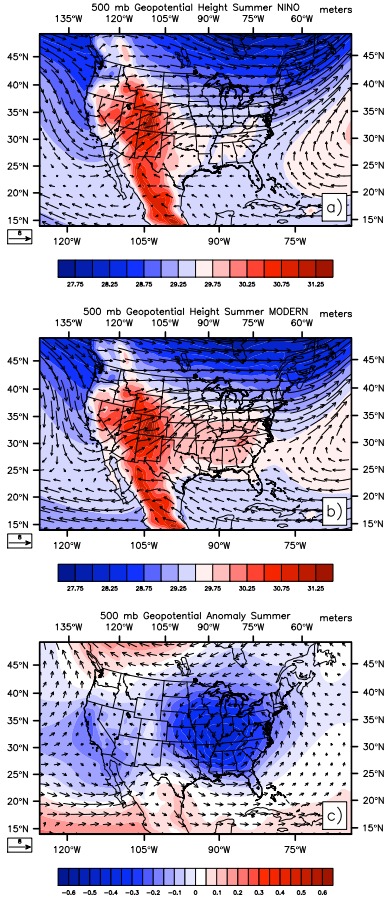

Fig. 12. Geopotential height anomaly (500 mb) and the mean wind as vectors plotted at 500 mb pressure surface. Plot **(a)** is the NINO case, plot **(b)** is the MODERN case, and plot **(c)** is the anomaly between the cases.

CPD
7, 199–240, 2011

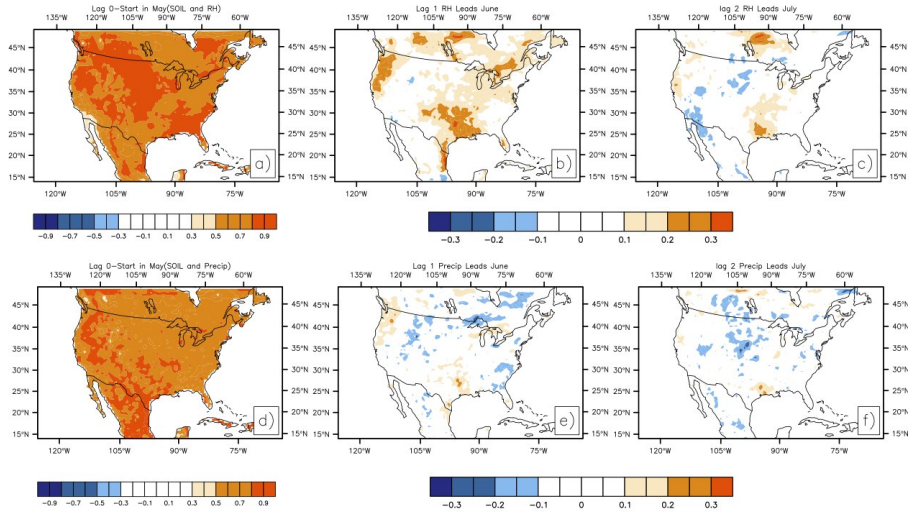

Fig. 13. Shows the correlation between soil moisture (SM) for the topmost layer in (mm) and fraction of relative humidity (RH) in plots **(a–c)** and soil moisture correlated against total precipitation in plots **(d–f)**. Correlations are plotted with lag of zero **(a)** which represents the climatological average for May–August (SM) versus May–August (RH), relative humidity lagging by one month **(b)** May–August (SM) versus June–Sseptember (RH), and lagging by 2 months **(c)** May–August (SM) versus July–November (RH). Plot **(d)** shows the correlation between soil moisture (mm) and total precipitation (mm day^{-1}) for lag 0 May–August (SM) versus May–August (precipitation), plot **(e)** is the correlation between soil moisture and total precipitation (May-August versus June–September), and plot **(f)** is the correlation of soil moisture and precipitation (May–August versus July–November).

CPD
7, 199–240, 2011